Inorganic Chemistry Communications 142 (2022) 109701

Contents lists available at ScienceDirect

Inorganic Chemistry Communications

journal homepage: www.elsevier.com/locate/inoche

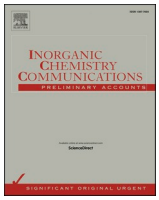

Short communication

Hydrothermal production of low-cost $CeNi_2S_4$-reduced graphene oxide composites as an efficient counter electrode for high performance dye-sensitized solar cells

K. Paramasivaganesh [a,b], D. Sakthilath [c], A. Sankar [c], P. Siva Karthik [d,*], Mohd. Shkir [e,f], F. Maiz [e,g], Woo Kyoung Kim [h,*], Sreedevi Gedi [h,*]

[a] Department of Chemistry, Arumugam Pillai Seethai Ammal College, Thiruppathur, Sivagangai District 630211, Tamil Nadu, Inidia
[b] Kandaswami Kandar's College, P. Velur, Namakkal, Tamil Nadu, India
[c] Department of Chemistry, Kandaswami Kandar's College, P. Velur, Namakkal 638182, Tamil Nadu, India
[d] Department of Chemistry, University College of Engineering, Panruti 607 106, Tamil Nadu, India
[e] Department of Physics, Faculty of Science, King Khalid University, P.O. Box 9004, Abha 61413, Saudi Arabia
[f] Department of Chemistry and University Centre for Research & Development, Chandigarh University, Mohali-140413, Punjab
[g] Laboratory of Thermal Processes, Center for Energy Research and Technology, Borj-Cedria, BP: 95, Tunisia
[h] School of Chemical Engineering, Yeungnam University, Gyeongsan 38541, Republic of Korea

ARTICLE INFO

Keywords:
$CeNi_2S_4$/rGO
Counter electrode
Charge-transfer process
Electrocatalysis
DSSCs

ABSTRACT

Dye sensitized solar cell (DSSC) technology could become a low-cost solution for solar energy harvesting if the use of expensive dyes and Pt can be avoided. This work reports the development of a novel nanohybrid based on $CeNi_2S_4$ nanotubes embedded on sheets of reduced graphene oxide (RGO), which can serve as excellent counter electrode for DSSC showing great promise to replace Pt. The structural and morphological characterization of the nanocomposite synthesized using a simple one step hydrothermal method revealed well defined crystalline nanotubes of $CeNi_2S_4$ (with length 190 nm and diameter 8.54 nm) uniformly embedded on the surfaces of the RGO sheets (~2.65 μm in size). The morphology and size of the nanotubes were found to be dependent on the duration of the hydrothermal reaction. The optimized $CeNi_2S_4$/RGO nanohybrid CE when used as counter electrode in DSSC, photo conversion efficiency as high as 9.21 ± 0.03 % was recorded, a value almost equal to that obtained from the DSSC fabricated with Pt as counter electrode and much higher than that with bare $CeNi_2S_4$ justifying its potential use in Pt-free DSSC. The improved performance of the electrode have been attributed to the hierarchical nanohybrid structure consisting of catalytically active 1D $CeNi_2S_4$ nanotubes embedded on electrically conducting 2D RGO sheets that provides fast ion diffusion pathways, large accessible surface area and good chemical and thermal stability.

1. Introduction

Over the past decade, there is an increasing interest in renewable energy technologies due to the combination of increasing world energy demand and fast depletion of traditional energy sources [1,2]. Amongst the different renewable energy, solar energy is of interest due to its practicality and abundant source [3,4]. Generally, the solar cell technology can be separated into three types, crystalline silicon, thin film and nanotechnology-based solar cells [5,6]. At the moment, the market leading technology is crystalline silicon due to its long lifetime (>25 years) and high power conversion efficiency (PCE) ~ 22% [7]. However, crystalline silicon based solar cells are expensive to its heavy material reliance and energy-intensive manufacturing process. It would be attractive to realize a lower cost solar cell with simple fabrication process. Consequently, mesoscopic dye-sensitized solar cells (DSSC) have been proposed due to their acceptable PCE and low material cost [8]. In addition, DSSCs can be manufactured at a plastic-compatible temperature using roll-to-roll fabrication process [9,10], which further reduce the overall manufacturing process. Typically the DSSC configuration consists of a dyed TiO_2 thin film, electrolyte, catalyst counter electrode clamped between two conductive glass substrates [11,12]. The counter electrode (CE) is an important component in DSSCs as it collects

* Corresponding authors.
E-mail addresses: psivakarthick@yahoo.com (P. Siva Karthik), wkim@ynu.ac.kr (W.K. Kim), drsrvi9@gmail.com (S. Gedi).

https://doi.org/10.1016/j.inoche.2022.109701
Received 25 April 2022; Received in revised form 16 June 2022; Accepted 19 June 2022
Available online 22 June 2022

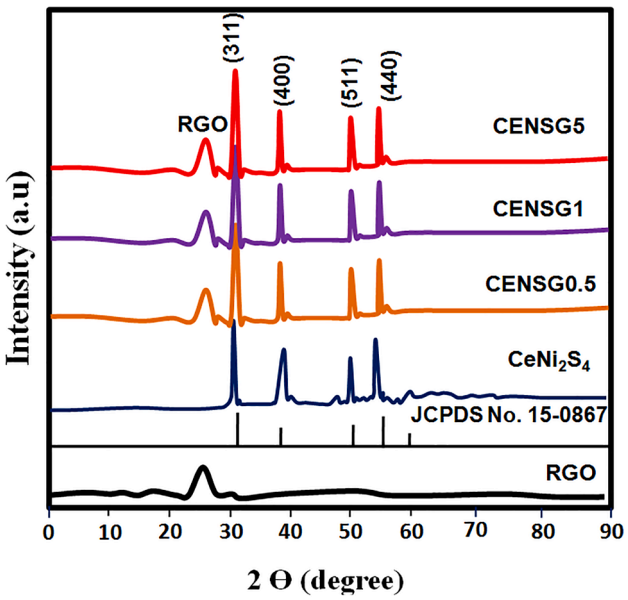

Fig. 1. (a) X-ray diffraction pattern; (b) crystal structure of $CuNi_2S_4$.

electrons from the external circuit and catalyzes the reduction of electrolyte [13]. The CE in DSSCs are typically made with Pt (it possess high conductivity, chemically stable against the electrolyte and highly electrocatalytic on FTO glass [14,15]. However, Pt is rare and which cost and therefore would be impractical for industrial production of DSSCs [16,17]. Therefore, it is important to find a more economical alternative CE for DSSCs with similar electrocatalytic performance. Researchers have considered various allotropes of carbon material [18], conductive polymers [19], metal nitride [20], metal sulfides [21] and metal selenide [22].

Owing to excellent catalytic activity and good chemical stability, transition metal oxides and sulfides have been frequently tested as CE material in DSSC. In particular, cobalt and nickel based mono and bimetallic sulfides have received large research attention in recent years since both Ni and Co have excellent redox properties suitable for large pseudocapacitance. Binary nickel cobalt sulfides can offer richer redox reactions than their corresponding single-metal sulfides owing to the contributions of both nickel and cobalt with different valence states. Sulfides also have relatively higher electrical conductivity compared to their oxide counterparts which make charge transport easier and faster than the oxides. In order to further improve the performance of metal sulfide/oxide based electrodes, researchers have often combined them with nanostructured carbon materials such as graphene, RGO or carbon nanotube, which have good electrical conductivity as well as large specific surface area [23,24]. S. Lu et al., reported highly efficient MoS_2/rGO electrocatalysts for triiodide reduction as Pt-free counter electrode for dye-sensitized solar cells [25]. A. Sarkar and his group reported $CoNi_2S_4$-reduced graphene oxide nanohybrid. The optimized $CoNi_2S_4$/RGO nanohybrid film when used as counter electrode in DSSC, photo conversion efficiency as high as 9.22% was recorded, a value almost equal to that obtained from the DSSC fabricated with Pt as counter electrode and much higher than that with bare $CoNi_2S_4$ justifying its potential use in Pt-free DSSC [26]. The combination of RGO and these materials could take advantage of the high electron transport ability of RGO and the abundant active sites of micro-nano structured materials, thus enhance the efficient electrocatalytic performance of the compounds. However, it has rarely been reported that the mixture of RGO and $CeNi_2S_4$ based materials applied as efficient and large-scale CE in DSSCs. In view of the above, here we report the synthesis of a nanohybrid CE consisting of $CeNi_2S_4$ nanotubes embedded on RGO nanosheets for use in DSSC. The prepared CE demonstrated that effectively improved electrocatalytic performance and stability as CE in DSSCs. Due to the combination of abundant active sites and superior conductivity, the $CeNi_2S_4$/RGO films reduced the interface resistance and electrolyte, promoted electron transfer, thus enhanced activity with a PCE of 9.21 ± 0.3% in DSSCs.

2. Experimental section

2.1. Chemical reagent

Expandable graphite flakes were purchased from KaiYu Industries, Nanjing, China. Sodium nitrate ($NaNO_3$), potassium permanganate ($KMnO_4$), sulfuric acid (H_2SO_4, 98%), hydrogen peroxide (H_2O_2, 30%), nickel nitrate hexahydrate (Ni $(NO_3)_2$, $6H_2O$), sodium hydroxide (NaOH), ethylene glycol, isopropyl alcohol, acetonitrile anhydrous, polyethylene glycol were bought from Merck, India. Ceriumt nitrate hexahydrate ($Ce(NO_3)_2$, $6H_2O$), l- cysteine, N-methyl-2-pyrrolidone, nafion (NR50), titanium dioxide nanopowder (purity > 99.5%, average particle size 21 nm), polyvinylidene fluoride (PVDF), lithium iodide (LiI), lithium per chlorate (LiClO4), iodine, N719 dye, and fluorine doped tin oxide (FTO) coated glass slides (sheet resistance ~7 Ω/sq)

2.2. Fabrication of RGO and $CeNi_2S_4$/RGO thin films

Firstly, graphene oxide (GO) was synthesized by a modified Hummer's method starting from expandable graphite flakes using $NaNO_3$, $KMnO_4$, H_2SO_4 and H_2O_2. Then the as synthesized GO was dispersed in 40 ml ethylene glycol (0.5 mg/ml) under ultrasonication. After 15 min of ultrasonication the GO solution was transferred to a magnetic stirrer where it was stirred for a further 20 min before adding 0.5 g of Ce $(NO_3)_2$,$6H_2O$ and 0.8 g of Ni$(NO_3)_2$,$6H_2O$ (1:2 M ratio) under stirring. After 2 h of stirring the solution mixture was transferred to a 100 ml teflon lined stainless steel autoclave and kept in a hot air oven at 160 °C for 24 h. To eliminate influence of temperature, it was kept constant for all the batches as it can also affect the size and shape of the particles. After that the autoclave was cooled to room temperature naturally and then the final product was washed several times with distilled water and ethanol followed by drying in vacuum at 60 °C for 8 h. The quantity of graphene in the $CeNi_2S_4$/RGO composites was regulated to be 0, 0.5, 1, and 5 wt% during the composite sample manufacturing procedure, and the corresponding samples were denoted as CENS, CENSG0.5, CENSG1, and CENSG5, respectively. When the reaction mixture was transferred to the autoclave, an acidic solution was formed because of Ce^{2+} and Ni^{2+} hydrolysis with the OH^- ions of water. Then an anion exchange reaction occurred in which the anions (OH^- and NO_3^{2-}) of the Ni—Co precursors were exchanged with the abundant S^{2-} ions, produced by the decomposition, to form the Co—Ni—S species. In the next step, these Co—Ni—S species nucleated on the solute (RGO) particles (sheets) and grew as $CeNi_2S_4$ nanotubes.

2.3. Fabrication of CE, photoanode and DSSC

The CE was made by mixing of $CeNi_2S_4$/RGO nanohybrid (80 wt%), acetylene black (10 wt%) and PVDF (10 wt%) by grinding them together and then dissolving in N-methyl-2-pyrrolidone (NMP) following common protocol. NMP was used mainly as a solvent to dissolve/disperse the nanohybrid as it is known to be an extremely good polar aprotic solvent that is miscible with water and hence can be easily removed from the film. PVDF was used as a binder to improve adhesion between the nanohybrid particles as well as to the FTO substrate. This prevents the film to come off from the FTO coated glass during repeated cyclic measurement. Acetylene black was used as a conductive additive and is widely used in non-metallic electrodes. The as-prepared slurry was then deposited on FTO glass to make a uniform film over an area of 2.5 cm × 2.5 cm by spin coating at 4000 rpm (Apex Instruments, India) followed by drying in air at 100 °C. For comparison, CEs were also made by using

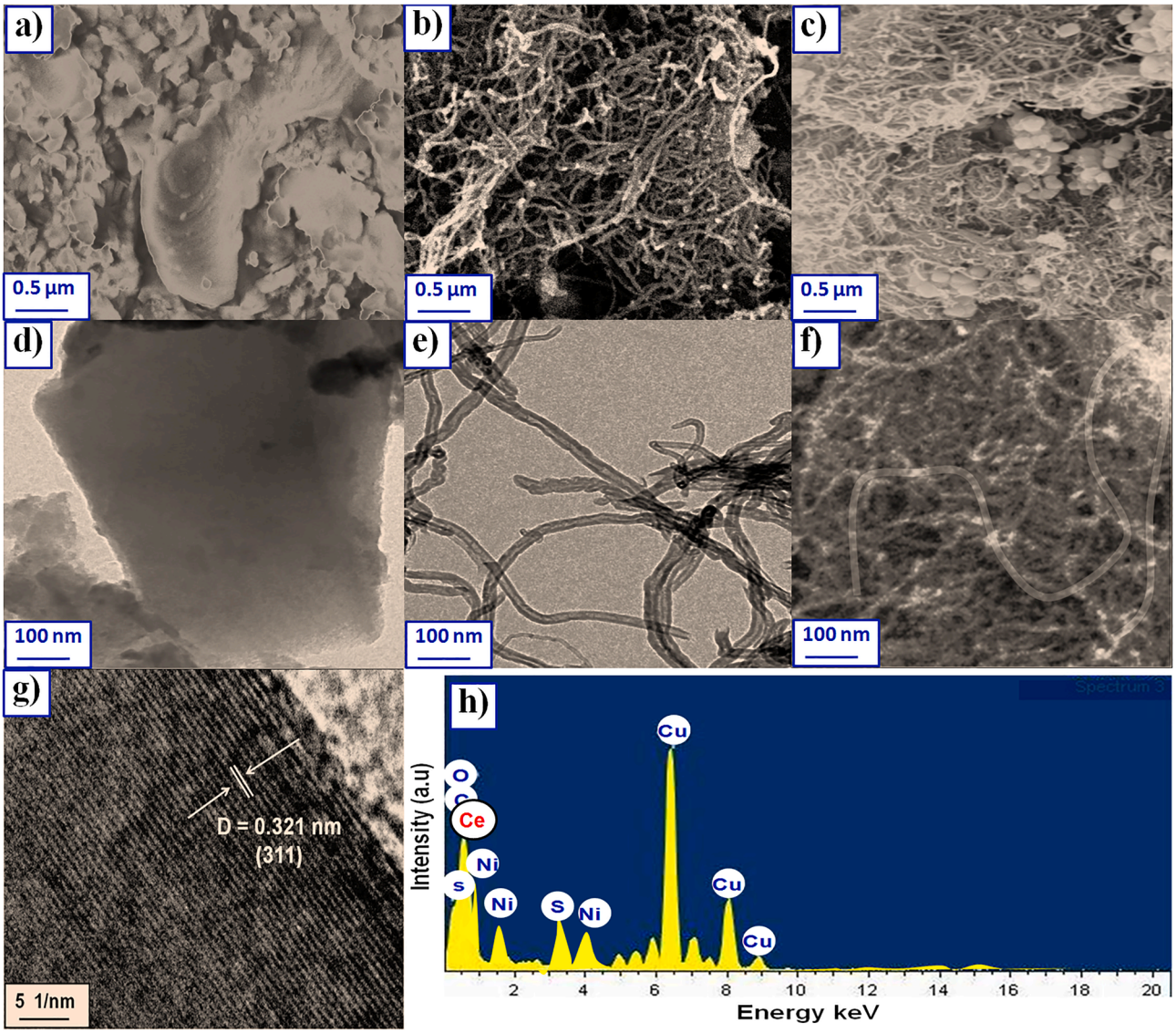

Fig. 2. SEM images of **a)** rGO; **b)** $CuNi_2S_4$; **c)** CUNSG5; TEM images of **d)** rGO; **e)** $CuNi_2S_4$; **f)** CUNSG5; **g)** HRTEM image of CUNSG5 and **h)** EDS of CUNSG5.

bare $CeNi_2S_4$ and bare RGO following the same procedure as above. The TiO_2 photoanode films were prepared using a commercial TiO_2 sol (Solaronix, Ti-Nanoxide T/SP) on FTO with the aforementioned method. To obtain dye-sensitized TiO_2 photoanodes, the films were soaked in the Ruthenium complexes dye solution (N719) dissolved in anhydrous ethanol for 24 h. All DSSCs were fabricated by using identical TiO_2 film based photoanode, N719 dye and identical electrolyte (0.05 M I2, 0.1 M LiI, and 0.1 M LiClO4 and dissolved in anhydrous acetonitrile) but using different CE material. For comparison, one DSSC device was also fabricated with a Pt film as CE.

2.4. DSSC device testing

The photocurrent density vs. voltage (J–V) characteristic of the DSSCs was recorded using a Keithley 2400 source meter connected across the photoanode and the counter electrode under the illumination of AM1.5 G solar light (100 mW/cm^2) using a CT50AAA solar simulator supplied by Photo Emission Tech, Inc., USA. The active device area during photovoltaic measurements was 20 mm × 20 mm while the aperture size of the mask was 22 mm × 22 mm. The thickness of the photoanonde and counter electrode was 1 and 0.8 µm, respectively. The light intensity was calibrated using a NREL based reference Si cell before the measurements. Upto 10 devices were tested to check the reproducibility and reliability of the device made with the optimized CE material.

3. Results and discussion

3.1. X-ray diffraction (XRD) analysis

The XRD pattern was utilized to describe the phase transition and crystal structure of several CEs in order to precisely examine them. Fig. 1 shows the XRD pattern of all the CEs. The peak position of bare rGO was found at 2θ of 26.47°, which could be indexed to (0 0 2) crystalline plane of GO. The pattern of $CeNi_2S_4$ appeared four various with sharp intense peaks (31.8°, 38.5°, 50.6°, 55.7°), which matched to the (3 1 1), (4 0 0), (5 1 1), (4 4 0) crystal planes. According to the standard vale (JCPDS No. 15-0867 card) the results are exactly matched to cubic phase of $CeNi_2S_4$. In can be seen that the high peaks in the spectrum all belong to $CeNi_2S_4$, indicating that the material had good crystallinity and purity. The material's crystal strength was linked to the intensity of the peaks. All of the distinctive peaks of $CeNi_2S_4$/RGO correlate well with those of RGO and $CeNi_2S_4$/RGO. This shows that $CeNi_2S_4$ has grown well on the rGO surface. The existence of RGO peaks in the composite sample suggests that throughout the hydrothermal process, RGO was successfully

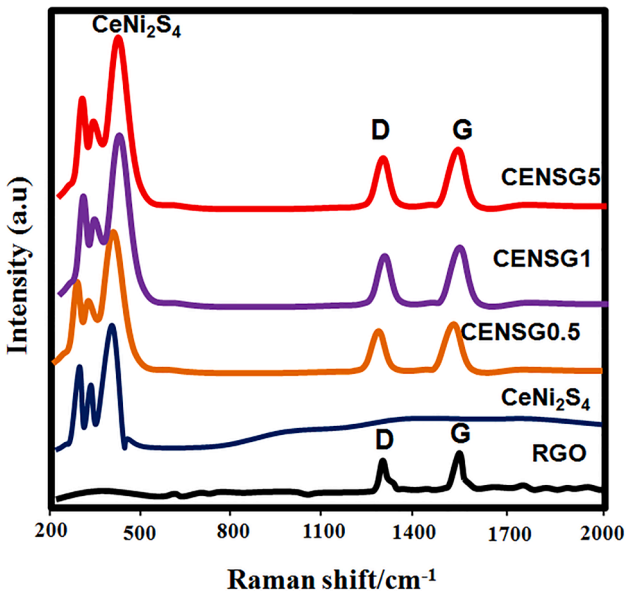

Fig. 3. Raman spectra of the thin film samples.

reduced from GO.

3.2. Morphological analysis

Morphological information of the prepared CEs is analyzed by SEM and TEM. Fig. 2 (a-c) SEM images of RGO, $CeNi_2S_4$ and CENSG5, samples, respectively. SEM images of bare RGO (Fig. 2a) and $CeNi_2S_4$ (Fig. 2b) shows sheets and well-defined long tube like structures with average length of 0.7 μm and average diameter of 70 nm Although, only few in number, these nanotubes like structures were found to shrink in their size compared to that in the bare $CeNi_2S_4$ suggesting that the presence of RGO restricts its overgrowth and results in lowering of the size of $CeNi_2S_4$ nanotubes in the CENSG5 sample (Fig. 2c). The TEM image of rGO shows clear 2D like with wrinkle type sheets (Fig. 2d). $CeNi_2S_4$ nanotubes were further identified the low magnification TEM images (Fig. 2e). The diameter of nanotubes was found to be 20–30 nm and length up to several micrometers. The uniform size nanotubes were successfully decorated on the surface of rGO sheets in the composite sample (Fig. 2f). The clear lattice fringes vale of about 0.321 nm in the HRTEM image further suggest that (311) orientation plane of cubic structure $CeNi_2S_4$ (Fig. 2g). Ce, Ni, S, and C are all present in the $CeNi_2S_4$/RGO composite sample EDS picture (Fig. 2h), indicating that RGO was successfully incorporated into $CeNi_2S_4$.

3.3. Raman spectra analysis

The Raman spectrum of the as-prepared $CeNi_2S_4$/RGO nanocomposite is presented in Fig. 3 along with the spectrum of bare RGO and $CeNi_2S_4$. $CeNi_2S_4$ shows the presence of prominent Raman peaks around 280, 332, and 376 cm^{-1}, which could be assigned to E_{1g}, A_{1g}, and E_{2g} vibrational modes of S atoms with respect to Ce-Ni atom, respectively [27]. The $CeNi_2S_4$/RGO nanocomposite also exhibits the same characteristic Raman peaks as that of $CeNi_2S_4$ and, in addition to these peaks, this composite also displays Raman peaks around 1344 and 1584 cm^{-1}, which originate due to the D-band and G-band of RGO, respectively [28]. The presence of the D-band and G-band confirms the presence of reduced graphene oxide (RGO) in $CeNi_2S_4$/RGO nanocomposite. Thus, Raman results also confirm the successful fabrication of $CeNi_2S_4$/RGO nanocomposite. In addition, the I_D/I_G values of RGO and RGO/$CeNi_2S_4$ films were 1.08 and 1.18, respectively. The effective decorating of RGO in the $CeNi_2S_4$ crystal matrix explains the difference in I_D/I_G value

3.4. Optical properties

To confirm the tunability of the optical properties of the $CeNi_2S_4$/RGO nanocomposite, UV absorption spectroscopy was used (Fig. 4a). The absorption spectrum of RGO shows a peak at about 280 nm, which originates from the π–π* transitions in the aromatic C—C bonds of the reduced graphene oxide. The $CeNi_2S_4$ absorption spectrum located at 410 nm. The light response was weak in the visible light spectrum, which is consistent with its catalytic activity. The absorption edge at 420 nm was greatly lowered when the amount of RGO was raised, and the absorption intensity in the visible range was also greatly raised (485 nm), indicating that the usage of light had been improved further. According to the Tauc plot [29,30], the optical bang gap was obtained and values are 3.02, 2.88, 2.81 and 2.71 eV for $CeNi_2S_4$, CENSG0.5, CENSG1, and CENSG5, respectively (Fig. 4b). The decreasing the band gap of composite sample is caused a significant increase in absorbance in the visible region emphasizing the synergistic effect of RGO and $CeNi_2S_4$. This is due to the band gap excitation of electrons from the valence band to the conduction band due to the presence of RGO and Ce. Ce atoms act

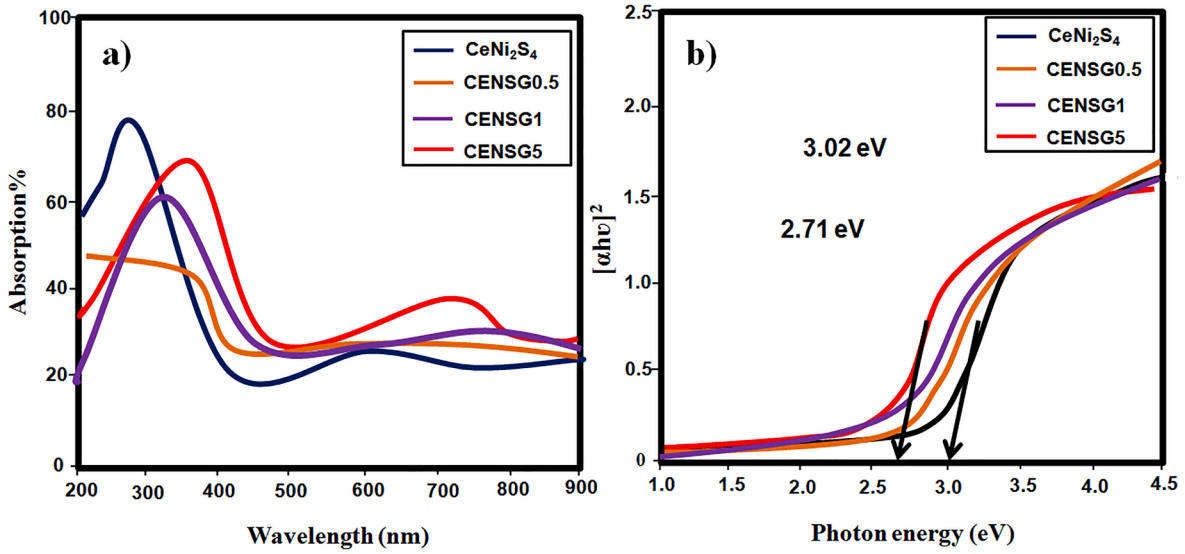

Fig. 4. a) UV–Vis absorption spectra and **b)** corresponding Tauc plot.

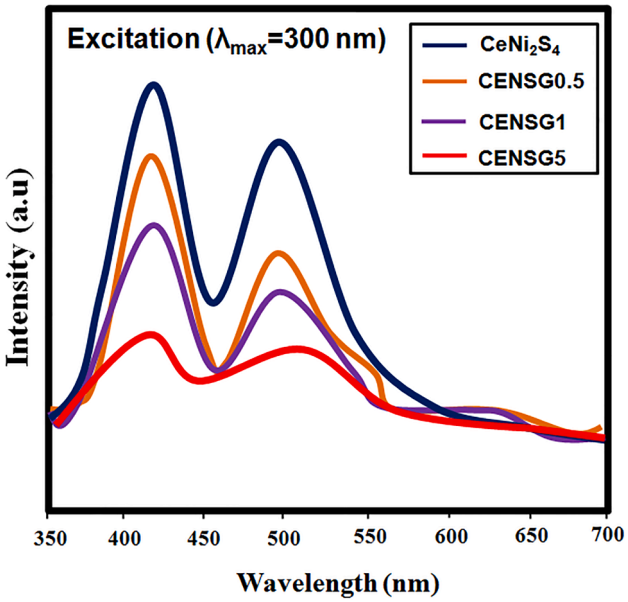

Fig. 5. Photoluminescence spectra of the thin film samples.

as electron trapping centers that result in a non-radiative recombination of electrons and holes. This means that the photoelectrons are preferentially transferred to the dopant level formed by Ce. As more Ce-Ni enters the crystal lattice, sulfur ions are displaced creating native Ce-Ni vacancies. So in order to prepare a solar driven DSSC $CeNi_2S_4$/RGO with small bandgap, the relative amount of Ce in the composite is very important to prevent electron–hole recombination. Fig. 5 shows the photoluminescence spectra of all CE samples stimulated at 300 nm. Photoluminescence spectra, which are generated by the recombination of free carriers, can provide further knowledge on the energy levels of imperfections in semiconductors and are commonly used to determine the bandgap energy. At 420 and 490 nm, two emission peaks were recorded. The emission maxima were measured at 2.95 and 2.53 eV, respectively, in the energy bandgap. The near band-edge emission (NBE) was attributed to these emission peaks, showing that the free electrons are reprocessed. Moreover, the gradual decreased emission was noticed when the loading of RGO increases, which could be due to recombination of electron-hole pair process was suppressed.

3.5. Textural analysis

The surface areas of the samples were measured by recording the adsorption–desorption isotherms against N_2 gas which are shown in Fig. 6. BET measurements show that incorporation of RGO largely influences the surface area of the nanohybrid samples show much larger values of specific surface area compared to that of the bare $CeNi_2S_4$ nanotubes. This is very much in accordance with expectation since RGO is known to have large surface area due to its planar structure. The constant isothermal temperature lines (type III, Brunauer-Deming-Deming-Teller classification) and hysteresis loops (H3, International Union of Pure and Applied Chemistry classification) identified in the BET spectrum on the left demonstrate the mesoporous nature of the materials [31–33]. While bare $CeNi_2S_4$ nanotubes exhibited specific surface area of only 58 m^2/gm and pore size of 16.2 nm, for $CeNi_2S_4$/RGO (CENSG5) nanohybrid it increased to 94 m^2/gm. The highest specific surface area of $CeNi_2S_4$/RGO (CENSG5) sample is the combined contribution of planar RGO sheets having large surface area and the formation of significantly smaller sized $CeNi_2S_4$ nanotubes than that in other samples.

3.6. Photovoltaic and photocurrent response

The fabricated DSSC set up was expressed schematically in Fig. 7a). The photovoltaic characteristics of DSSCs assembled with bare RGO, bare $CeNi_2S_4$, $CeNi_2S_4$/RGO and Pt film as CE were evaluated under full sunlight illumination (100 mW/cm^2, AM1.5 G), and the data for the best performing devices are presented in Fig. 7 (b) whereas the corresponding photovoltaic parameters of merit obtained for those DSSCs are summarized in Table 1. It can be seen that DSSCs made with bare RGO as CE shows a rather low FF and PCE as a result of its poor electrocatalytic property. For DSSC with bare $CeNi_2S_4$ as CE, the Jsc and FF value increases slightly because of its comparatively better catalytic activity, leading to enhanced PCE value of 5.77 ± 0.02 % from 3.45 ± 0.01%. For DSSCs made with $CeNi_2S_4$/RGO (CENSG5) CE the values of photovoltaic parameters further enhanced because of the synergistic effect of electrically conducting RGO and catalytically active $CeNi_2S_4$ nanotube like structures but due to disordered morphology and presence of mixed phases of $CeNi_2S_4$, the DSSCs made with them displayed relatively low FF and PCE value. The PCE value of 9.21 ± 0.03 % was obtained for the best performing DSSC made with $CeNi_2S_4$/RGO (CENSG5) as CE which is very close to the PCE value (9.18%) of the DSSC made with Pt as CE. The initial increase in J_{SC} and V_{OC} can be explained by the formation of

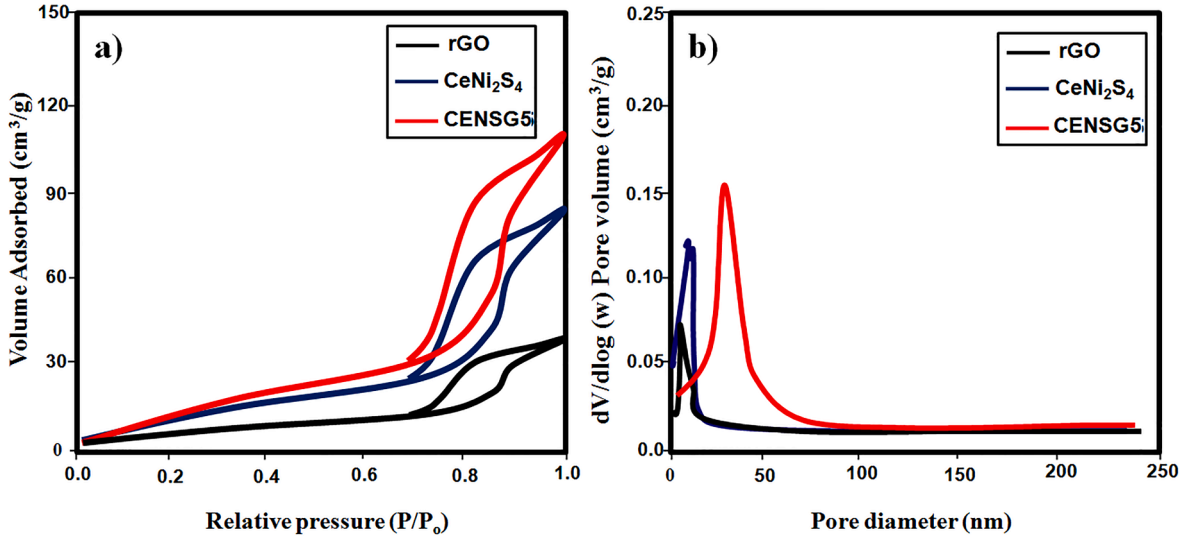

Fig. 6. a) N_2 adsorption and desorption analysis rGO, $CuNi_2S_4$ and CUNSG5 films. **b)** corresponding pore size distribution.

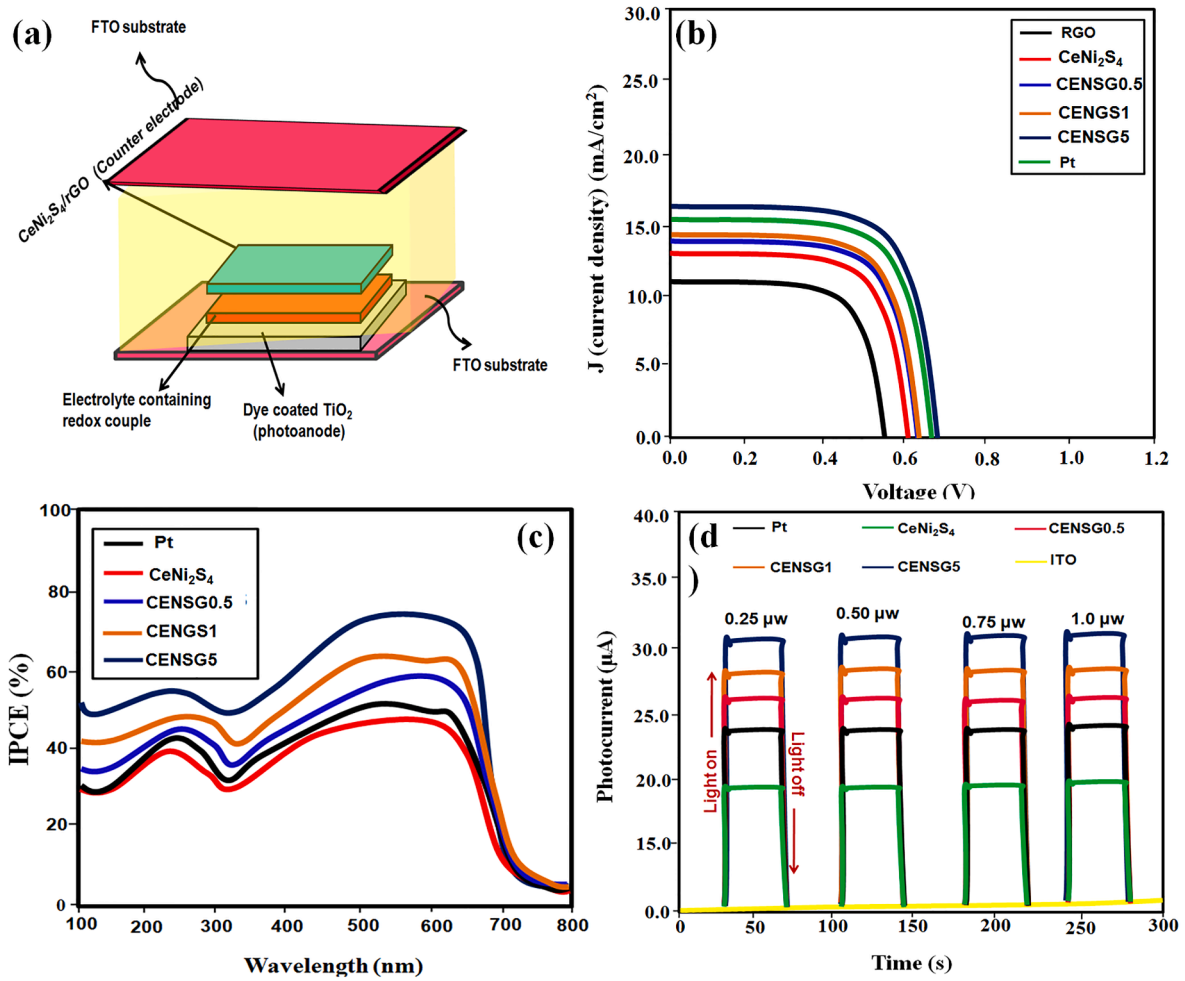

Fig.7. a) Schematic representation of the fabricated DSSC; **b)** J-V plot **c)** IPCE spectra; **d)** Transient photo response curve.

Table 1
Photovoltaic parameters of all the CEs.

Parameters	RGO	$CeNi_2S_4$	CENSG0.5	CENSG1	CENSG5
Jsc (mA/cm^2)	10.68 ± 0.02	13.64 ± 0.02	14.12 ± 0.02	15.76 ± 0.02 16.56 ± 0.02	
Voc (V)	0.55 ± 0.01	0.61 ± 0.01	0.63 ± 0.01	0.67 ± 0.01	0.69 ± 0.01
Fill Factor	58 ± 0.02	72 ± 0.02	75 ± 0.02	0.71 ± 0.02	084 ± 0.02
PCE η (%)	3.45 ± 0.01	5.77 ± 0.01	6.36 ± 0.01	7.71 ± 0.01	9.21 ± 0.03

*Data for each cell are based on five individual samples with standard deviation

more conductive sites by RGO, which considerably decreases the transport resistance for photogenerated electrons. The J_{SC} corresponds to the ejected electron numbers throughout the external circuit, while V_{OC} is associated with the difference between the Fermi level of $CeNi_2S_4$ under illumination and the Nernst potential of the I^-/I_3^- redox couple in the electrolyte [34]. The change in V_{OC} of the DSSC, based on $CeNi_2S_4$ and $CeNi_2S_4$/RGO CEs, shows that the Fermi level of the $CeNi_2S_4$/RGO CEs is affected by the RGO incorporation. Compared with other fabricated electrodes, $CeNi_2S_4$/RGO (CENSG5) sample exhibited the highest fill factor and short circuit current (Jsc) which can be attributed to the numerous small size nanotubes well distributed and well anchored on RGO sheets (having large surface area) forming not only good conducting pathways, but also improving catalytic performance leading to faster reduction of I_3^- to I^- (due to increased surface catalytic sites). The I^- ions in turn promotes the regeneration of dyes, thus injecting more photoelectrons, and suppressing the inner circuit recombination, all of which lead to the highest value of Jsc and FF in the photovoltaic tests. Fig. 7c) shows the IPCE spectra of all the CE thin films. In order to draw a contrast, the IPCE spectra might also be combined to yield the comparable value of the short-circuit current density (J_{IPCE}). J_{IPCE} values for Pt, $CeNi_2S_4$, CENSG0.5, CENSG1, and CENSG5, DSSCs are 10.68, 13.14, 13.89, 14.86, 16.34 and 16.31 mA/cm^2, correspondingly, which are close to JSC findings derived using J-V curves. The varying current densities of several CEs were represented in Fig. 7d (transient photocurrent response, I-T) under the same light source excitation and numerous switching cycles. The researchers came to the conclusion that conductive glass (ITO) was just a technique for finding the current response intensity of CE materials. It lacked the capacity to create electricity. The current ability was quickly noticed once any type of catalytic substance was applied to ITO. The relevant current density improved significantly when the composite CEs were produced by adding various quantities of RGO. The best-performing ($CeNi_2S_4$/RGO-5% current density increased by more than five times that of bare $CeNi_2S_4$. In addition, Fig. S1 shows long-term stability data of a bare $CeNi_2S_4$ and $CeNi_2S_4$/RGO (CENSG5) based DSSC under continuous AM 1.5 G irradiation. It is found that the value of PCE gradually decreases from its initial value to 88% after irradiation for 60 days, which can be ascribed to the adsorption of water molecules on carbon based CEs. In subsequent tests, the cell efficiency becomes stable. This result indicates that the $CeNi_2S_4$/RGO based DSSC shows reasonable stability in long-term operation. On the other hand, the aperture of the mask on the DSSC should be large enough to avoid shadowing of the active area and

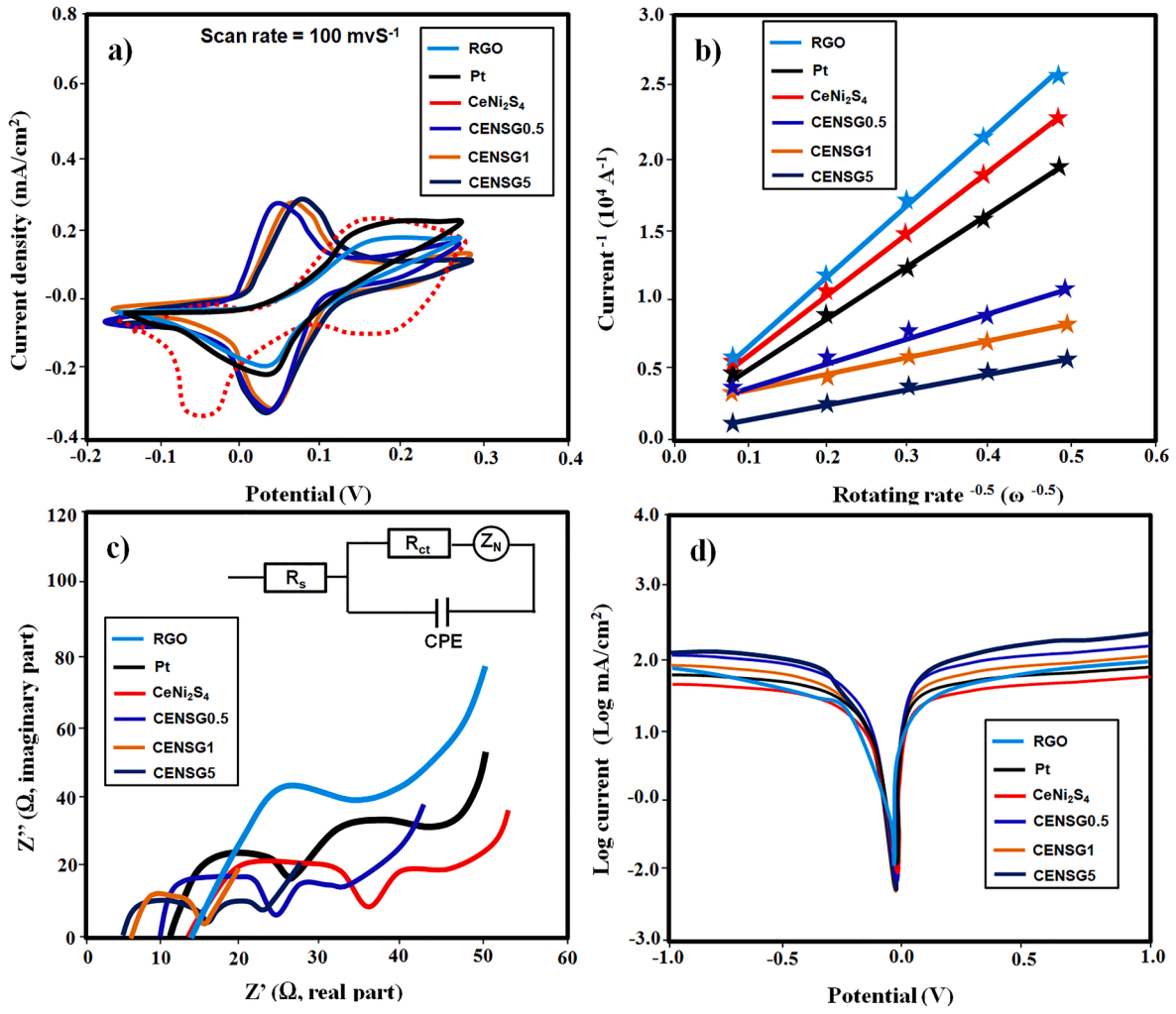

Fig. 8. **a)** CV curves of all the CEs; **b)** Plots of i^{-1} vs. $\omega^{-0.5}$ of the various CEs; **c)** Nyquist plot and **d)** Tafel polarization of all the CEs.

Table 2
EIS parameters of all the CEs.

Parameters	Pt	$CeNi_2S_4$	CENSG0.5	CENSG1	CENSG5
K_0 ($x10^{-2}$ cm/s)	1.61	2.45	2.51	2.66	2.77
|Ipc| ($mAcm^{-2}$)	3.12 ± 0.02	2.77 ± 0.02	3.34 ± 0.02	3.55 ± 0.01	3.77 ± 0.02
R_S ($\Omega\ cm^{-2}$)	12.21 ± 0.02	14.15 ± 0.02	10.13 ± 0.02	8.91 ± 0.04	6.81 ± 0.01
R_{CT} ($\Omega\ cm^{-2}$)	21.61 ± 0.01	19.84 ± 0.01	16.31 ± 0.01	14.97 ± 0.01	12.68 ± 0.02
J_0 ($mAcm^{-2}$)	1.12	1.05	2.45	3.89	5.89
IPCE (%)	44	42	61	64	78

Table 3
Comparison results of PCE between present work and already reported works.

Sample	Method	Dye	PCE (%)	Ref.
MoS/GO	Electrodeposition	N719	8.01	[42]
SnS/GO	Solvothermal	N719	3.91	[43]
rGO-$NiCo_2S_{4-1}$	Solvothermal	N719	7.06	[44]
rGO-$NiCo_2S_4$	Co-pricipitation	N719	6.01	[45]
MoS/CNT	Solvothermal	N719	8.40	[46]
$CeNi_2S_4$/RGO	Hydrothermal	N719	9.21	this work

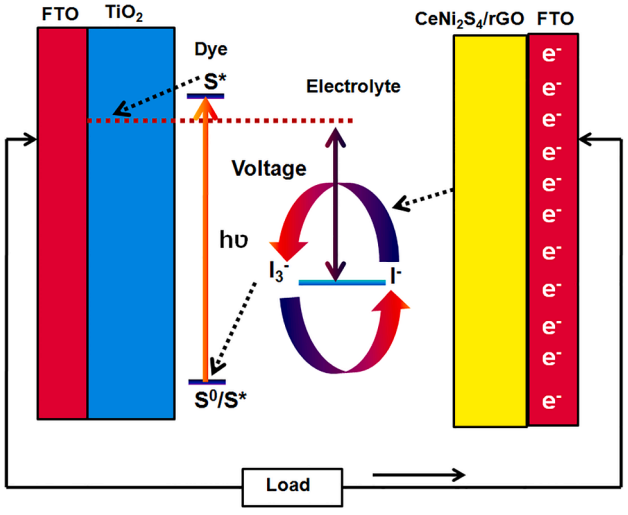

Fig. 9. Schematic representation of the photo-conversion mechanism of the $CuNi_2S_4$/rGO hybrid films under solar light irradiation.

restriction of the angle for reception of diffuse radiation. The large drop in JSC observed in Fig. S2 by changing the configuration from (c) to (b) can be attributed to the latter unwanted effect. In quantitative terms the loss of JSC is influenced by the relative content of diffuse radiation in the

simulator and other geometrical factors. The fact that the present cell combines a large distance (4 mm) between the mask and the photoactive film with a small active area (the side length of the electrode is 3 × 5 mm) renders this configuration particular susceptible to the effects of restricting the reception angle for diffuse light. in Fig. S2 where the increase in aperture are of the mask from 16 to 36 mm^2 for a device size of 12 × 2 mm^2 did not affect the photocurrent density, suggesting that any contribution of light collection from the small inactive area of exposed TCO glass to the photocurrent is below experimental error. It may be suggested that the collection of light from the inactive part of a photovoltaic DSC module, for example, the area occupied by interconnects or current collector grids could be exploited as a means to raise the total area conversion efficiency of the device. While this idea is valid in principle the data in Fig. S2 show that if the inactive surface is constituted only by a narrow strip of TCO glass, there are no significant benefits to be expected from this effect. Other light management strategies, for example, the use of scattering particles would have to be employed to enhance the harvesting of sunlight striking photo-inactive parts of the solar cell.

3.7. Electrochemical properties

Both cyclic voltammetry (CV) and rotating disc electrode (RDE) methods were utilized in this work to investigate the electrochemical characteristics of the CEs in more depth. At a scan rate of 100 mV/s, cyclic voltammograms of the electrodes with films of Pt, $CeNi_2S_4$, CENSG0.5, CENSG1, and CENSG5 are shown in Fig. 8a). For evaluating the electrocatalytic capacities of CEs, the peak to peak separation (Epp), cathodic current density (Ipc), and potential (Vpc) were important metrics [35,36]. The catalytic ability of CEs was favourably associated with the |Ipc| among them. The |Vpc| and |Epp| were independently associated linked with the electrocatalytic activity of CEs. According to Fig. 8a, the $CeNi_2S_4$/rGO-5% CE had an even higher |Ipc| (3.77 ± 0.02 $mAcm^{-2}$) than the $CeNi_2S_4$, CENSG0.5, and CENSG1 CEs, and was slightly higher than the Pt CE (3.12 ± 0.02 $mAcm^{-2}$), suggesting that the $CuNi_2S_4$/RGO CE effectively created an opportunity in the I^-/I_3^- electrolytes. Moreover, the simplified Kouteck- Levich equation [37] was utilized to statistically quantify the functional electrochemical surface area (A_e) and the conventional heterogeneous rate constant (k_0) using a rotating disc electrode (RDE). According to the Fig. 8b) and Table 2 shows that $CeNi_2S_4$/rGO-5 % CE has a higher k_0 of 2.77 × 10^{-2} cm^2/s than $CeNi_2S_4$ (2.45 × 10^{-2} cm^2/s) and bare Pt (1.61 × 10^{-2} cm^2/s); this is attributable to the porous structure and electrical conductivity of rGO, as well as the efficient electrochemical property of $CeNi_2S_4$ for the conversion of I_3^- ions to I^- ions. Complementary EIS was also used to assess CE behaviour. Fig. 8 c) and inset show Nyquist plots of the CEs and equivalent circuit. Two semicircles can be seen: the semicircle at high frequencies reveals the existence of resistant in the charge transfer (Rct) activity at the electrode/electrolyte contact and determines the catalytic activity of CEs; the semicircle at low frequencies demonstrated the formation of resistance in the charge transport (Rct) activity at the electrode/electrolyte contact and describes the catalytic activity of CEs. In low frequency, the second semicircle also specifies the dispersion resistance at the electrode contact. The addition of rGO in the $CuNi_2S_4$ nanohybrid with the lowest Rct accelerates charge transfer and improves electrocatalytic performance significantly (see Table 2). Tafel polarization studies reveal much more about electrocatalytic activity of the CEs that have been produced. The symmetric cells in the dark were used to record Tafel curves (Log J plotted vs. voltage) employing linear sweep voltammetry at low scan rates (Fig. 8d). Table 2 contains data generated from Tafel plots for various CEs. The cell built with $CuNi_2S_4$/rGO/FTO electrodes had the maximum current density, demonstrating the nanohybrid's capacity to catalyse the I_3^-/I^- redox process. We found that the trends of the f_{max} and J_0 values are similar, following the sequence of $CeNi_2S_4$ > CENSG0.5 > CENSG1 > Pt > CENSG5. The obtained results indicate the trends of τ and *J0* were similar to those found for the *Rct* values. Note that a shorter τ indicates a faster electron transfer across the CE/electrolyte interface [38] and that a high J_0 value indicates a high short-circuit current density (*Jsc*) in DSCs [39–41]. Moreover, the PCE obtained in the present work is comparatively high than other metal sulfides/graphene oxide based materials [42–46]. The results are summarized in Table 3.Solar-driven interfacial evaporation has been developed in the past decade and received great achievements. Until now, the highest PCE is reported to be even over 100% for the combination of both materials and structural designs. The developed $CeNi_2S_4$/RGO hybrid composite materials are applied for SSG devices. As a result, as-prepared materials have micrometer-sized pores with an excellent broadband absorption, low heat capacity, and low heat conductivity. The highest η was up to 85% and the steam generation rate was 1.55 kg $m^{-2}h^{-1}$ for $CeNi_2S_4$/RGO with a 1–2 μm pore size under one sun solar simulation (Fig. S3). The improved performance of $CeNi_2S_4$/RGO sample is due to high surface area with a pore size of micrometers was better than that of samples with a pore size of nanometers. This may be associated with the viscosity of water suppressed in nanosized pore channels, resulting in sluggish delivery of water to hot regions [47–49]. Fig. 9 depicts the photo conversion mechanism. The J-V and electrochemical data imply that the RGO might increase PCE and electrocatalytic activity greatly. This might be because combining $CuNi_2S_4$ with a sufficient quantity of RGO rapidly increases reaction species on the composites and improves electron transport at the electrode/electrolyte interface, resulting in increased in electrocatalytic activity. When compared to the Pt counter electrode, the $CeNi_2S_4$–5 wt% RGO CE shows better electrocatalytic activity for I_3 reduction. Furthermore, raising the RGO level above 5% had no effect on electrode function. One possibility might be that higher levels of RGO disrupt the development of $CeNi_2S_4$ nanostructures and their equivalent to increasing with RGO. This might have an impact on the $CeNi_2S_4$ and RGO synergistic interactions necessary for quicker electron transport at the electrode–electrolyte interface, resulting in better electrocatalytic activity in the DSSC.

4. Conclusions

A facile and one-pot hydrothermal method was used to prepare a hybrid composite of $CeNi_2S_4$/RGO as the electrocatalytic film for the counter electrode of a dye-sensitized solar cell. The structure and morphology of the corresponding samples were characterized by XRD, TEM Raman spectra and XPS. All the characteristic results of $CeNi_2S_4$/RGO indicating the success of growth for $CeNi_2S_4$ on the surface of rGO. Electrochemical studies such as EIS, Tafel polarization and CV delivered reliable evidence of excellent electrocatalytic activities of the $CeNi_2S_4$/RGO hybrids. Remarkably, the DSSC fabricated with a composite of $CeNi_2S_4$ and 5 wt% RGO (CENSG5) showed a power conversion efficiency of 9.21 ± 0.03 %, which was higher than that of Pt (9.18 ± 0.01 %). The $CeNi_2S_4$/RGO composite thin films may stand out as a competitive alternative to the expensive platinum counter electrode due to the good electrocatalytic property acquired from the cheap cost and simple production procedure.

Declaration of Competing Interest

The authors declare that they have no known competing financial interests or personal relationships that could have appeared to influence the work reported in this paper.

Acknowledgements

The author would like to express their gratitude to Deanship of Scientific Research at King Khalid University, Abha, Saudi Arabia for funding this work through Research Group Program under Grant No. R.G.P.2/123/43. We also appreciate and acknowledge the support of Priority Research Centers Program through the National Research Foundation of Korea (NRF) funded by ministry of Education (Grant No:

2014R1A6A1031189).

Appendix A. Supplementary material

Supplementary data to this article can be found online at https://doi.org/10.1016/j.inoche.2022.109701.

References

[1] I.Y.Y. Bu, T.-H. Hu, The role of various carbon nanomaterials for dye-sensitized solar cells applications, Sol. Energy 130 (2016) 81–88.
[2] G. Palai, A. Nayyar, R. Manikandan, B. Singh, Metamaterial based photonic structure: an alternate high performance antireflection coating for solar cell, Optik. 179 (2019) 740–743.
[3] I.Y.Y. Bu, Y.-S. Fu, J.-F. Li, T.-F. Guo, Large-area electrospray-deposited nanocrystalline Cu XO hole transport layer for perovskite solar cells, RSC Adv. 7 (74) (2017) 46651–46656.
[4] T.V. Luu, N.S. Nguyen, Parameters extraction of solar cells using modified JAYA algorithm, Optik. 203 (2020), 164034.
[5] T. Markvart, L. Castañer, Principles of solar cell operation, McEvoy's Handbook of Photovoltaics, Elsevier, 2018, pp. 3–28.
[6] I. Dharmadasa, Advances in Thin-film Solar Cells, CRC Press, 2018.
[7] A. Zhang, Z. Guo, Efficient light trapping in tapered silicon nanohole arrays, Optik. 127 (5) (2016) 2861–2865.
[8] F. Bella, C. Gerbaldi, C. Barolo, M. Grätzel, Aqueous dye-sensitized solar cells, Chem. Soc. Rev. 44 (11) (2015) 3431–3473.
[9] J.M. Pringle, V. Armel, D.R. MacFarlane, Electrodeposited PEDOT-on-plastic cathodes for dye-sensitized solar cells, Chem. Commun. 46 (29) (2010) 5367, https://doi.org/10.1039/c0cc01400a.
[10] H.C. Weerasinghe, F. Huang, Y.-B. Cheng, Fabrication of flexible dye sensitized solar cells on plastic substrates, Nano Energy 2 (2) (2013) 174–189.
[11] I.Y.Y. Bu, M.T. Cole, One-pot synthesis of intercalating ZnO nanoparticles for enhanced dye-sensitized solar cells, Mater. Lett. 90 (2013) 56–59.
[12] J. Gong, K. Sumathy, Q. Qiao, Z. Zhou, Review on dye-sensitized solar cells (DSSCs): advanced techniques and research trends, Renew. Sustain. Energy Rev. 68 (2017) 234–246.
[13] Q. Tang, J. Duan, Y. Duan, B. He, L. Yu, Recent advances in alloy counter electrodes for dye-sensitized solar cells. A critical review, Electrochim. Acta 178 (2015) 886–899.
[14] V. Sugathan, E. John, K. Sudhakar, Recent improvements in dye sensitized solar cells: a review, Renew. Sustain. Energy Rev. 52 (2015) 54–64.
[15] I.Y.Y. Bu, Sol-gel derived cobalt sulphide as an economical counter electrode material for dye sensitized solar cells, Optik. 127 (19) (2016) 7602–7610.
[16] E. N, G. G, A. S, R. P, R. P, Effect of tin oxide crystallite size on the efficacy of polyaniline-tin oxide nanocomposite based counter electrode for DSSC applications, Optik. 142 (2017) 436–445.
[17] J. Theerthagiri, A.R. Senthil, J. Madhavan, T. Maiyalagan, Recent progress in non-platinum counter electrode materials for dye-sensitized solar cells, Chem. Electro. Chem. 2 (2015) 928–945.
[18] W.J. Lee, E. Ramasamy, D.Y. Lee, J.S. Song, Performance variation of carbon counter electrode based dye-sensitized solar cell, Sol. Energy Mater. Sol. Cells 92 (7) (2008) 814–818.
[19] K. Saranya, M.d. Rameez, A. Subramania, Developments in conducting polymer based counter electrodes for dye-sensitized solar cells–an overview, Eur. Polym. J. 66 (2015) 207–227.
[20] G.R. Li, J. Song, G.L. Pan, X.P. Gao, Highly Pt-like electrocatalytic activity of transition metal nitrides for dye-sensitized solar cells, Energy Environ. Sci. 4 (5) (2011) 1680, https://doi.org/10.1039/c1ee01105g.
[21] J. Huo, J. Wu, M. Zheng, Y. Tu, Z. Lan, High performance sponge-like cobalt sulfide/reduced graphene oxide hybrid counter electrode for dye-sensitized solar cells, J. Power Sources 293 (2015) 570–576.
[22] K.S. Lee, H.K. Lee, D.H. Wang, N.-G. Park, J.Y. Lee, O.O. Park, J.H. Park, Dye-sensitized solar cells with Pt-and TCO-free counter electrodes, Chem. Commun. 46 (25) (2010) 4505, https://doi.org/10.1039/c0cc00432d.
[23] N. Chakrabarty, A.K. Chakraborty, Controlling the electrochemical performance of β-$Ni(OH)_2$/carbon nanotube hybrid electrodes for supercapacitor applications by La doping: A systematic investigation, Electrochim. Acta 297 (2019) 173–187.
[24] N. Chakrabarty, A.K. Chakraborty, H. Kumar, Nickel hydroxide nanohexagon based high performance electrode for supercapacitor: a systematic investigation on the influence of six different carbon nanostructures, J. Phys. Chem. C 123 (2019) 29104–29115.
[25] S. Lu, M. Chen, Y. Wang, R. Li, J. Lin, X. Zhang, Highly efficient MoS_2/rGO electrocatalysts for triiodide reduction as Pt-free counter electrode for dye-sensitized solar cells, Sol. Energy 220 (2021) 788–795.
[26] A. Sarkar, S. Bera, A.K. Chakraborty, $CoNi_2S_4$-reduced graphene oxide nanohybrid: An excellent counter electrode for Pt-free DSSC, Sol. Energy 208 (2020) 139–149.
[27] K.N. Sudesh, S. Das, C. Bernhard, G.D. Varma, Effect of graphene oxide doping on superconducting properties of bulk MgB_2, Supercond. Sci. Technol. 26 (2013), 095008.
[28] E.P. Randviir, D.A.C. Brownson, J.P. Metters, R.O. Kadara, C.E. Banks, The fabrication, characterisation and electrochemical investigation of screen-printed graphene electrodes, PCCP 16 (2014) 4598.
[29] X. Wang, K. Maeda, A. Thomas, K. Takanabe, G. Xin, J.M. Carlsson, K. Domen, M. Antonietti, A metal-free polymeric photocatalyst for hydrogen production from water under visible light, Nat. Mater. 8 (2009) 76.
[30] M. Parthibavarman, K. Vallalperuman, S. Sathishkumar, M. Durairaj, K. Thavamani, A novel microwave synthesis of nanocrystalline SnO_2 and its structural optical and dielectric properties, J. Mater. Sci.: Mater. Electron. 25 (2) (2014) 730–735.
[31] R. BoopathiRaja, M. Parthibavarman, Hetero-structure arrays of $MnCo_2O_4$ nanoflakes@nanowires grown on Ni foam: Design, fabrication and applications in electrochemical energy storage, J. Alloy. Compd. 811 (2019), 152084.
[32] R. BoopathiRaja, M. Parthibavarman, A. Nishara Begum, Hydrothermal induced novel $CuCo_2O_4$ electrode for high performance supercapacitor applications, Vacuum 165 (2019) 96.
[33] M. Parthibavarman, M. Karthik, S. Prabhakaran, Facile and one step synthesis of WO_3 nanorods and nanosheets as an efficient photocatalyst and humidity sensing material, Vacuum 155 (2018) 224.
[34] V.-D. Dao, S.-H. Kim, H.-S. Choi, J.-H. Kim, H.-O. Park, J.-K. Lee, Efficiency Enhancement of Dye-Sensitized Solar Cell Using Pt Hollow Sphere Counter Electrode, J. Phys. Chem. C 115 (51) (2011) 25529–25534.
[35] E. Sim, E. Park, V.-D. Dao, H.-S. Choi, Synthesis of PtSe catalysts using atmospheric-pressure plasma and their application as counter electrodes for liquid-junction photovoltaic devices, Catal. Today 337 (2019) 126–131.
[36] Y.Y. Duan, Q.W. Tang, J. Liu, B.L. He, L.M. Yu, Transparent Metal Selenide Alloy Counter Electrodes for High-Efficiency Bifacial Dye-Sensitized Solar Cells, Angew. Chem. Int. Ed. 53 (2014) 14569.
[37] J.-Y. Lin, W.-Y. Wang, S.-W. Chou, Flexible carbon nanotube/polypropylene composite plate decorated with poly(3,4-ethylenedioxythiophene) as efficient counter electrodes for dye-sensitized solar cells, J. Power Sources 282 (2015) 348–357.
[38] A.J. Bard, L.R. Faulkner, Electrochemical Methods: Fundamentals and Applications, John Wiley & Sons Inc, New York, 2001.
[39] Hai-Linh Thi Dang, Van-Duong Dao, Vu Ngoc Hung, Vu Hong Ha Thi, Tran Nam Anh, Nguyen Thi Khanh Huyen, Xuan-Co Hoang, Nguyen Thi Hanh, Phạm Anh Tuan, Micro-wheels composed of self-assembled tungsten oxide nanorods supported platinum counter electrode for highly efficient liquid-junction photovoltaic devices, Solar Energy 214 (2021) 214–219.
[40] Hai-Linh Thi Dang, Nam Anh Tran, Van-Duong Dao, Vu Ngoc Hung, Dang Viet Quang, Vu Hong Ha Thi, et al., Carbon nanotubes-ruthenium as an outstanding catalyst for triiodide ions reduction, Synthetic Metals. 260 (2020).
[41] V.-D. Dao, H.-L. Dang, N.H. Vu, H.H.T. Vu, N.D. Hoa, N.V. Hieu, P.A. Tuan, Nanoporous NiO nanosheets-based nanohybrid catalyst for efficient reduction of triiodide ions, Sol. Energy 197 (2020) 546–552.
[42] S. Li, H. Min, F. Xu, L. Tong, J. Chen, C. Zhu, L. Sun, All electrochemical fabrication of MoS_2/graphene counter electrodes for efficient dye-sensitized solar cells, RSC Adv. 6 (2016) 34546–34552.
[43] I.Y. Bu, Solvothermal production of low-cost tin sulfide microsphere/reduced graphene oxide nanocomposite as counter electrode for dye-sensitized solar cells, Optik. 182 (2019) 658–663.
[44] K.S. Anuratha, M. Ramaprakash, S.K. Panda, S. Mohan, Studies on synergetic effect of rGO-$NiCo_2S_4$ nanocomposite as an effective counter electrode material for DSSC, Ceram. Int. 43 (2017) 10174–10182.
[45] J. Han, Q. Luo, X. Yin, H. Lin, Z. Yao, X. Zhao, Y. Zhou, H. Nan, X. Li, Economically synthesized $NiCo_2S_4$/reduced graphene oxide composite as efficient counter electrode in dye-sensitized solar cell, Appl. Surf. Sci. 437 (2017) 227–232.
[46] L. Gu, Z. Yu, M. Wu, X. Li, W. Zhang, X. Zhao, L. Li, X. Zhang, D. Wang, Q. Zhang, Electrospinning synthesis of high performance carbon nanofiber coated flower-like MoS_2 nanosheets for dye-sensitized solar cells counter electrode, Electrochim. Acta 280 (2018) 94–100.
[47] V.-D. Dao, D.C. Nguyen, W. Stręk, Nguyen Duc Chien, Wiesław Strek, Enthusiastic discussions on solid physic and material science at SPMS2019, Sci. Technol. Develop. J. 23 (2) (2020) 490–498, https://doi.org/10.32508/stdj.v23i2.1768.
[48] V.-D. Dao, Ngoc Hung Vu, Sining Yun, Recent advances and challenges for solar-driven water evaporation system toward applications, Nano Energy 68 (2020), 104324.
[49] Y. Ito, Y. Tanabe, J. Han, T. Fujita, K. Tanigaki, M. Chen, Multifunctional Porous Graphene for High-Efficiency Steam Generation by Heat Localization, Adv. Mater. 27 (29) (2015) 4302–4307.